2-1-2007

Design of a Flexible Centering Tooling System

Laine Mears
Clemson University, mears@clemson.edu

Francis M. Kolartis

Michael Thompson

Thomas R. Kurfess

Design of a Flexible Centering Tooling System

Introduction

Precise machining of bearing rings is integral to the quality of assembled bearings. The output accuracy of center-based machining systems such as lathes or magnetic chuck grinders can relate directly to the accuracy of part centering before machining. Traditionally, such machines achieve centering by either hard tooling to which the ring is pressed, or through manual centering by a skilled operator using a brass hammer. Hard tooling has the problems of being subject to wear, dimensional inaccuracy, and additional setup time at part type changeover. Manual centering methods are subject to human error, both in accuracy and repeatability. Whether through setup time or manual centering time, either method requires skilled labour and is relatively expensive.

To address this concern, an automated centering tooling system is proposed that will:

- Automatically approach a ring held by gravity to a rigid rotating plate and follow its outer surface based on sensor input
- Gather and filter data of the ring surface location relative to the spindle angle
- Extract the vector of center of geometry offset from the center of rotation
- Provide actuation force to the ring at a position and manner to move its geometrical center to the center of spindle rotation

Author

- Use the residual error of previous pushes to modify the actuation command for subsequent pushes

Design targets are:

- Minimisation of centering error
- Minimisation of centering time
- Minimisation of implementation cost
- Minimisation of operator skill requirement
- Ability to center rings from 0.5 to 70kg

For such a tooling system to be effective in meeting design targets, especially those of minimising centering error and time, the physical mechanisms of part movement must be properly understood. Primarily, modeling and control of friction-dominant systems, actuator path planning and control, and the dynamics of pushing and impact interactions of rigid bodies must be accounted for in the system design.

Previous Work

Friction Modeling

There has been extensive work on modeling friction in mechanical systems. A number of models have been proposed, linear and nonlinear, continuous and discontinuous, each applicable in one or more domains or velocity regimes. The simplest is the Coulomb model of friction:

$$F_C = \mu F_N \qquad (1)$$

where the friction force F_C is proportional to the normal force F_N by the static friction coefficient μ [Åström (1998)]. Though used successfully in practice, this model gives rise to discontinuity and does not account for dynamic behaviour (velocity-dependent friction). Therefore, a number of augmentations and separate modeling schemes have been developed.

Bliman and Sorine developed a group of dynamic friction models to account for velocity-dependent behaviour [Åström (1998)]. LuGre extended the model of Dahl to capture frictional properties such as stick-slip (known as *stiction*) and frictional time lag [Åström (1998)]. Dupont, Armstrong and Hayward (2000) have developed a dynamic model that captures both stiction and observed presliding displacement. The model of de Wit, Olsson and Åström (1995) brings together most experimentally observed effects: the Stribeck effect, hysteresis, the spring-like behaviour of stiction, and variation in the static friction force.

More recently, there has been work to capture frictional effects for small displacement actuation of rigid bodies. Ferrero and Barrau (1997) specifically study friction under small displacement and near-zero velocity. This is a highly nonlinear regime not modeled by Coulomb, but directly applicable to this project. Mirtich and Canny (1995) have created a dynamic simulation environment completely based on the impulse

contact model, where all forms of actuation (pushing, sliding, impact) are modeled by a series of collisions.

Control of Frictional Systems

The above models have been applied directly in control schemes for systems with appreciable friction. The model of deWit (1995) is explored to develop new control strategies for frictional systems, including observer-based control. Hirschorn and Miller (1997) present a new continuous dynamic controller for application to systems modeled on the dynamic nonlinear model of LuGre, and successfully apply it to a high-speed linear positioner. Alvarez, Garrido and Femat (1995) developed a control strategy based on accurate friction force estimation. Olsson and Åström (2001) as well as Dupont (1991) have developed friction control systems specifically targeted to avoid stiction-induced limit cycling behavior, a condition where stiction causes a system to continually overshoot its desired state.

Actuation by Pushing

Not only are system stability and control important in frictional systems, but also the ability to deterministically modify the system. One example is actuation of a sliding object to a desired position.

Peshkin and Sanderson (1988) described the motion of a sliding workpiece for all possible pressure distributions on the support surface. Zesch and Fearing (1998) explore force-controlled pushing for microparts with positional results in the 1μm range. Lynch and Mason (1992,1995) have done extensive work on planning and control for stable pushing in the application of robotic manipulation as an alternative to pick-and-place positioning, including feasibility studies through both kinematic and force analyses (1996). Lynch (1999) also explores open-loop control for pushing the general polygonal shape, characterised by the "maneuverability" property.

Actuation by Tapping

Huang and Mason (2000) have studied manipulation of sliding objects by imparting a momentum through impulsive actuation, then allowing the object to come to rest. Analysis of such actuation requires separate analysis of energy transfer during impact, then analysis of the free sliding motion with friction. Huang, Krotkov and Mason (1995) give a general solution to these problems (first *The Inverse Sliding Problem*, then *The Impact Problem*) to a rotationally symmetric class of objects, and present limiting cases of this application (1996). Yao, Chen and Liu (2005) have recently explored an energy-based coefficient of restitution for the planar impact problem.

Application of these concepts to impact-based static positioning systems is treated separately by Liu, Higuchi and Fung (2003) in their piezoelectric positioning table, as well as by Siebenhaar (2004) in electromechanical hammer control.

Positioning Tooling System Description

Hardware

The tooling system is based on a single measurement probe and actuator. It consists of an air-bearing spindle table upon which the subject part is placed and a linear motor air-bearing slide that carries the measurement probe and pusher tip.

During operation, the part is placed by hand onto the machine table and the spindle is rotated. The slide is advanced and commanded through a PID controller to follow the measurement probe signal. The position of the ring outer diameter is then measured and the signal modeled by a single-lobe sine function. This function is used to identify the center of geometry offset from the center of rotation. Finally, the ring is moved by a series of controlled impacts or pushes to align the centers.

The flexible tooling system is implemented on a National Instruments PXI-8176RT controller with a PXI-7350RT motion control board. PXI is an extension of the compact PCI bus architecture specific to instrumentation. This hardware allows for control loop rates up to 20 kHz with deterministic loop timing in a compact, rugged chassis.

The encoding resolutions of the slide and probe are 20nm and 50nm. These are implemented as Heidenhain linear encoders with incremental quadrature conversion. The encoding resolution of the spindle is 0.09° (4000 counts per revolution).

The prototype system is displayed in Figure 1.

Sensor Requirements

The design requirements of sensing in this application are:

- $\leq 0.1\mu m$ resolution. The centering tolerance target is $2.5\mu m$ and should be discriminated at least 10X. Provision for lower tolerances in the future should be guaranteed by this design constraint
- Minimise sensor cost. As this system is planned for application to existing equipment, cost is kept low to remain feasible.
- Minimise contact force. On lighter mass parts, sensor force can have an appreciable effect on actuation force, and in the worst case, sensor force alone can move the part undesirably. Ideally, sensor should not contact the part being measured (*i.e.*, zero force).
- Maximise sensor look-ahead capability. In order to initially approach the ring at maximum slide velocity, sensor look-

ahead should be maximised in order to provide adequate stopping distance after the part surface is detected.

- Sense parts of varying material, roughness, finish type, and color.

Spindle Angular Velocity

The angular velocity of the spindle is constrained by three limits:

1. The maximum angular velocity at which the part signal can be reliably sampled. This is determined by the frequency response of the probe and the maximum data acquisition rate. Nyquist sampling rules apply.

2. The maximum angular velocity at which a reliable push can be executed at the desired angular location.

3. The minimum centrifugal force that would overcome the work holding force. For a vertical spindle with gravity-based work holding, the work holding force is simply the static friction between the part and the worktable. The maximum angular velocity for this condition is derived from

$$F_{centr} = F_S$$

$$F_{centr} \equiv centrifugal\ \ force = m\omega_{\max}^2 e$$

$$m \equiv part\ mass[kg]$$

$$\omega_{\max} \equiv critical\ angular\ velocity\left[\frac{rad}{s}\right]$$

$$e \equiv eccentricity\ of\ \ centers[m]$$

$$F_S \equiv static\ \ friction\ \ force = \mu_s mg$$

$$\mu_s \equiv static\ \ friction\ coefficient$$

$$g \equiv gravitational\ acceleration = 9.807\,\frac{m}{s^2}$$

Solving for angular velocity,

$$\omega_{\max}[rpm] = \frac{60}{2\pi}\sqrt{\frac{\mu_s g}{e}} \qquad (2)$$

Conservatively assuming μ_s=0.05 and 25mm maximum eccentricity,

$$\omega_{\max} = 42.3\ rpm \tag{3}$$

The maximum angular velocity as limited by centrifugal force can be increased by increasing the work holding force through:

- Increased friction. The assumption of μ_s is quite conservative. Actual measurements of different rings on the prototype setup are in the range 0.15-0.25.
- Supplementing with magnetic work holding force. This can come from electromagnetic chucking force as on a grinding machine or by the addition of small subsurface magnets installed below the table rails. Magnetic work holding cannot be used on nonferrous parts.
- Supplementing with some other form of work holding force such as Coulomb force or compliant fluid or gel adhesives.
- Decreasing eccentricity of the part. As the part approaches center, eccentricity is decreased and the spindle speed can increase according to (2).

Sensor Stroke

Adequate stroke will allow for acceptable sensor look-ahead and stopping distance after encountering the part surface. This also provides for acceptance of large error between expected and actual operating conditions (*e.g.*, operator placement of incorrect ring type).

The instantaneous ring position along the line of action of the probe (see Figure 2) is

$$p(e,\omega,r,t) = e\cos(\omega t) + \sqrt{r^2 - e^2\sin^2(\omega t)} \tag{4}$$
$$r \equiv \textit{part radius}[m]$$

The approach velocity of the ring surface along the line of action of the probe is found by differentiating the position equation in time:

$$v_{ring}(t) = \frac{\partial}{\partial t} p(e,\omega,r,t) = -e\omega\sin(\omega t) - \frac{e^2\omega\sin(\omega t)\cos(\omega t)}{\sqrt{r^2 - e^2\sin^2(\omega t)}} \quad (5)$$

Assuming a maximum eccentricity of 25mm, a minimum part radius of 30mm and by (3),

$$v_{ring,\max} = 154.3\ mm/s \quad (6)$$

The maximum slide velocity is 120mm/s, and maximum slide acceleration is 2560mm/s^2. The maximum interference velocity is given by

$$\begin{aligned} v_{\max} &= v_{ring,\max} + v_{slide,\max} \\ v_{\max} &= 274.3\ mm/s \end{aligned} \quad (7)$$

Therefore the minimum stopping distance at full deceleration is

$$\begin{aligned} d_{\min} &= \frac{a_{\max} t^2}{2} \\ t &= \frac{v_{\max}}{a_{\max}} = \frac{274.3}{2560} = 0.11s \end{aligned} \quad (8)$$

$$d_{\min} = 14.7\ mm \quad (9)$$

Since this stopping distance decreases as part radius increases, the assumed case is the limiting case. The sensor look-ahead should be maintained longer than this distance to avoid a crash (unintentional part contact) condition.

Sensor Selection

Laser and confocal sensors were initially considered due to their noncontacting nature. However, based on our desired range these sensors were both cost-prohibitive and subject to reflectivity problems for differing ring treatments and finishes.

The initial sensor used with the system was an analog signal LVDT with 10mm range, 0.1μm resolution and 10V output. This component was acceptable from a design constraint standpoint, but introduced noise into the measurement signal by induction of the linear motor drive current.

The final sensor chosen is the Heidenhain MT2581 digital length gauge. This sensor incorporates a glass scale linear encoder, and minimises noise through filtering at quadrature decoding. The sensor has 25mm of stroke, 50nm resolution, and imparts a maximum 0.7N gauging force at full stroke. Assuming a static friction coefficient of μ_s=0.15, the minimum weight part able to be centered, assuming only gravity work holding, is 0.5kg, which is at the minimum of the desired applicability domain for the tooling system.

Software

This tooling control architecture is based on a real-time version of LabVIEW that allows for deterministic loop time control. Determinism in programming is defined as ability to complete a given operation in a fixed, known time.

The algorithm architecture is parallel loop, with each thread scheduled according to its priority:

- Control Loop (Highest Priority). PID control of servo command from measurement probe. This loop also contains the pushing code that activates when all push conditions are met.
- Data Collection Loop (High Priority). Logging of measurement probe tip data in relation to spindle position
- Data Modeling Loop (Normal Priority). Filtering of modeling queue and fitting to sine wave model, extraction of pushing parameters.
- Communication Loop (Lowest Priority). Transfer of values from PXI memory to user display on PC (front panel).

The algorithm is implemented directly on PXI hardware, so no PC is required, though one is used for monitoring system performance. The user interface is shown in Figure 3.

On the user interface, the Data plot displays raw data collected over a single spindle rotation, the Model plot displays the result of the last model loop cycle, and the polar plot tracks the last n (user-settable) models in r-θ form.

The control loop occurs at a 100 Hz rate. During each cycle, the probe position is read, the deviation from the null value calculated, and the slide velocity is commanded through a PID control scheme. Superposition of acceleration and deceleration curves is internal to the motion control software. When the push conditions are satisfied (modeling is complete and the spindle is in correct position), the part following routine is suspended and the deterministic pushing profile is loaded to the motion controller. After the push is complete, part following resumes.

The data collection loop occurs at 66 Hz, and logs the sum of the probe and slide positions. This data is paired with the instantaneous spindle positions to create a raw trace of the ring outer surface. The data is low-pass filtered to remove high frequency noise such as physical dirt and finish abnormalities as well as electrical noise affecting the probe signal.

The modeling loop becomes active when data collection has occurred over a full ring rotation. The entire filtered data set is fitted by a linear least squares algorithm to a single period sine wave function with a constant DC offset and a period of one spindle revolution. This allows extraction of the parameters used in pushing, namely off-center distance and angular

direction. This loop polls at 10 Hz, executing the modeling code when a full data set is available.

The final loop is the communication loop, which exchanges values between the PXI unit and the user PC. As this process is memory-intensive, these actions can be preempted by any other loop, and then resumed after higher-priority activities are complete.

Memory management of all loop activities and priorities is handled by the LabVIEW-RT runtime engine, which takes advantage of the PXI communication bus. This allows activities utilising different hardware (*e.g.*, data collection card, motion control card) to operate deterministically with respect to each other. This management code is included at compilation.

System Identification and Control of Measurement and Actuation Axis

The linear slide plant is modeled as a second-order frictionless system:

$$\begin{aligned} &m\ddot{x} = F(t) \\ &\quad m \equiv \textit{moving slide mass, including bracket and sensor} \\ &\quad \ddot{x} \equiv \textit{second time derivative of slide position} \\ &\quad F(t) \equiv \textit{input driving force function} \end{aligned} \tag{10}$$

Transforming to the Laplace domain,

$$ms^2 X(s) = F(s)$$

$$\frac{X(s)}{F(s)} = \frac{1}{ms^2} \tag{11}$$

This is a critically stable system for all gain values. The simulated response of the uncontrolled system in Figure 4 shows complete lack of following capability.

A controller was designed using the NI Control Design Toolkit with equal requirements of fast settling time and low percent overshoot. The PID controller was first simulated in LabVIEW, then directly implemented in the control algorithm. The final PID controller is of the form

$$G(s) = \frac{20s^2 + 5s + 25}{s} \tag{12}$$

Settling time for sinusoidal input less than 3Hz is under 2ms with no overshoot. The simulated time series plot in Figure 5 shows the extremely close tracking to the input signal.

This controller allows for rapid approach of the slide to the part and close following of the part surface during rotation, as well as rapid settling after each push in order to resume data collection.

Data Collection and Modeling

The measurement tip position is calculated from the linear slide and measurement probe encoder values. The slide convention is positive toward spindle center and the probe convention is positive away from spindle center. The tip position is given by

$$d_{tip} = d_{slide} - d_{probe} \tag{13}$$

Measuring tip data is collected relative to spindle radial position, so data pairs are in r-θ form. The (spindle position, tip position) data pairs include both process and measurement noise. Initial simulation with standard low-pass filtering (*e.g.*, Butterworth) resulted in introduction of undesirable phase lag, which could adversely affect the trajectory plan for ring movement. Therefore, the data are filtered using a Kalman optimal estimator gain filter, which allows adjustment of the weights of process and measurement error to minimise the phase lag while removing high frequency noise.

Kalman Filtering

The filter first presented by Kalman (1960) is an efficient recursive solution to optimally estimate the state of a process through the least-squares method. For a process state x with input u governed by the matrix equation

$$x_k = Ax_{k-1} + Bu_{k-1} + w_k \tag{14}$$

with an observed (measured) value of

$$w_k = Hx_k + v_k \tag{15}$$

w_k and v_k are process and measurement noise, distributed respectfully as

$$p(w) \sim N(0, Q)$$
$$p(v) \sim N(0, R)$$

where Q and R are covariances. The estimator for such a system is given by

$$\hat{x}_k = \hat{x}_k^- + K(z_k - H\hat{x}_k^-) \tag{16}$$

The covariance of the estimate error is given by

$$P_k \equiv E\left[(x_k - \hat{x}_k)(x_k - \hat{x}_k)^T\right] \tag{17}$$

The error covariance is minimised by substituting (16) into (17), differentiating with respect to K, setting equal to zero and solving for K. The residual weight K known as the *Kalman gain* is that which minimises the estimate error. Welch (2003) gives the derivation to be

$$K_k = \frac{P_k^- H^T}{HP_k^- H^T + R} \tag{18}$$

The implementation of the Kalman filter is of predictor-corrector form. In a single-input, single-output (SISO) scalar system with unity transformation of state and measurement (A=1, H=1) and no input contribution (B=0), the predictor step is

$$\hat{x}_k^- = \hat{x}_{k-1} \tag{19}$$

$$P_k^- = P_{k-1} + Q \tag{20}$$

Note that the best estimator of the state at the next time step is the state value at the previous time step, and process noise is introduced to the estimate error. This estimation set now undergoes correction based on the observed value by

$$K_k = \frac{P_k^-}{P_k^- + R} \tag{21}$$

$$\hat{x}_k = \hat{x}_k^- + K_k(z_k - \hat{x}_k^-) \tag{22}$$

$$P_k = (1 - K_k)P_k^- \tag{23}$$

This recursive predictor-corrector method marches forward in time as the system state updates and new measurements are taken. If the assumption that process and measurement covariances Q and R are constant is true, then the optimal gain will converge to a constant value K.

In the prototype setup, measurement noise covariance R was calculated from a data set taken by measuring a stationary object and found to be $(0.03\mu m)^2$. Process noise covariance Q was tuned for good filter performance, and finally determined to be $(0.015\mu m)^2$. This tuning gives beneficial smoothing of high-frequency physical noise (*e.g.*, dust, part finish), while allowing for accurate representation of lower-frequency part

manufacturing variation (e.g., multipoint lobe form from grinding) without appreciable phase lag.

As R is a property of the measurement device, it is assumed constant. Q is a property of not only the system setup, but also the specific ring being measured. However, after initial tuning it is held constant for all ring types. This assumption may be relaxed in future work, where Q may become an input variable to the part-specific software setup. Filter performance as implemented is simulated in Figure 6.

Process Modeling

After filtering, the data are fitted to a single period sine wave through a linear least squares fit model of the form:

$$y = b_0 + B\sin(x + \phi) \tag{24}$$

This can be expanded to

$$y = b_0 + b_1 \sin(x) + b_2 \cos(x)$$

Coefficients b_i are chosen to minimise the function

$$\chi^2 = \sum_{i=0}^{n-1} \left(\frac{y_i - \sum_{j=0}^{2} b_j H_j(x_i)}{\sigma_i} \right)^2$$

$$H_0 \equiv 1 \qquad (25)$$
$$H_1 \equiv \sin(x)$$
$$H_2 \equiv \cos(x)$$
$$\sigma_i \equiv \textit{std. deviation of random error of } y$$
$$\textit{assumed distributed} \sim N(0, \sigma^2)$$

From these coefficients, we can directly determine the direction ϕ and distance B of the ring eccentricity:

$$b_1 = B\cos(\phi)$$
$$b_2 = B\sin(\phi)$$

$$\cos^2(\phi) + \sin^2(\phi) = 1 = \frac{{b_1}^2 + {b_2}^2}{B^2}$$

$$B = \sqrt{{b_1}^2 + {b_2}^2} \qquad (26)$$

$$\tan(\phi) = \frac{\sin(\phi)}{\cos(\phi)} = \frac{b_2 / B}{b_1 / B}$$

$$\phi = \tan^{-1}\left(\frac{b_2}{b_1}\right) \qquad (27)$$

Actuation

Push Distance

The push distance is defined as the distance the slide must move in the forward direction in order to push the ring from its eccentric position to the center of rotation. The push distance is calculated from 3 components:

$$d = d_{gap} + d_{ampl} - d_{lead} \tag{28}$$

d_{gap} ≡ Distance to close gap between probe and pusher tip

d_{ampl} ≡ Distance to move the ring

d_{lead} ≡ Distance to compensate for leading the ring phase

These distances are graphically represented in Figure 7.

The distance to close the following gap is calculated directly from the difference between instantaneous probe position and known probe position when the probe is collapsed to the level of the pusher tip:

$$d_{gap} = d_{probe} - d_{probe,pushtip} \tag{29}$$

The distance to move the ring is equal to the amplitude of the sine model, determined from model coefficients:

$$d_{ampl} = \sqrt{b_1^{\,2} + b_2^{\,2}} \tag{30}$$

The distance to compensate for leading the ring phase is determined from geometry as seen in Figure 8.

$$d_{lead} = d_{ampl} + r - x$$

$$x \equiv d_{ampl}\cos(L) + r\cos(\alpha)$$

$$\alpha \equiv \sin^{-1}\left(\frac{d_{ampl}\sin(L)}{r}\right)$$

$$r \equiv \textit{part radius}$$

$$d_{lead} = d_{ampl} + r - d_{ampl}\cos(L) - r\cos\left(\sin^{-1}\left(\frac{d_{ampl}\sin(L)}{r}\right)\right)$$

$$d_{lead} = d_{ampl}(1-\cos(L)) + r\left[1-\cos\left(\sin^{-1}\left(\frac{d_{ampl}\sin(L)}{r}\right)\right)\right]$$

The final push distance is

$$d = d_{probe} - d_{probe,pushtip} + \sqrt{b_1^{\,2} + b_2^{\,2}}\cos(L) - r + \sqrt{r^2 - (b_1^2 + b_2^2)\sin^2(L)} \tag{31}$$

subject to

$$r > \sin(L)\sqrt{b_1^2 + b_2^2}\text{, or}$$

$$r > B\sin(L)$$

This is absolutely satisfied independent of rotational velocity when

$$r > B \tag{32}$$

More simply, the spindle center must initially be contained within the ring outer surface. Otherwise, the line of action of the probe will encounter a "no part" condition at some point during full rotation.

Pushing Velocity

Once the ring is in position to begin the push, servo following is suspended and the slide undergoes a fixed trapezoidal velocity move as shown in Figure 9.

The pushing occurs beginning with zero relative velocity between the ring and the top surface of the spindle. Moving the ring requires a discontinuous transition between static and kinetic friction as the ring starts to move. After breakaway, the required force drops, causing overshoot of the desired position, and possible return to zero velocity. This *stick-slip* motion is a common phenomenon occurring in frictional systems. (Åström 98) exemplifies this phenomenon with the simulation of a simple block of mass *x* pulled by a spring *y*, the behaviour of which is shown in Figure 10. The velocity of the block starts and stops, given a ramp input of the spring position.

The net result of stick-slip in this application is a limit cycling of the position control, causing the ring to experience back-and-forth actuation completely across the tolerance zone without convergence at small desired amplitudes (<200μm). An exaggerated case is presented in Figure 11.

To counteract the limit cycling condition for small actuation distances, an empirical push velocity function was developed to minimise this effect. This is accomplished by decreasing the constant velocity at impact exponentially as actuation distance decreases between pushes. The function is characterised by four parameters that can be set based on ring characteristics.

The function is of the form

$$v(d) = v_{\max} \cdot e^{-\left(\frac{d_{crit}-d}{d_{crit}}\right)^{1/s} \cdot \ln\left(\frac{v_{\max}}{v_{\min}}\right)}$$

when $d < d_{crit}$.

This is simplified to

$$v(d) = \begin{cases} v_{\min}^{\left(\frac{d_{crit}-d}{d_{crit}}\right)^{1/s}} \cdot v_{\max}^{1-\left(\frac{d_{crit}-d}{d_{crit}}\right)^{1/s}}, & d < d_{crit} \\ v_{\max}, & otherwise \end{cases} \quad (33)$$

where

v_{min} ≡ minimum allowable push velocity
v_{max} ≡ maximum allowable push velocity
d_{crit} ≡ minimum distance to push at max velocity
s ≡ "steepness" of decay curve when $d < d_{crit}$

The velocity function is graphically represented in Figure 12. For our current part mass range (0.75 – 1.5kg), function parameters were empirically selected as follows:

$$\begin{aligned} v_{\min} &= 400\frac{mm}{s} \\ v_{\max} &= 3500\frac{mm}{s} \\ d_{crit} &= 2500\mu m \\ s &= 1.0 \end{aligned} \tag{34}$$

This parameter set is that which achieved the best centering performance during experiments.

Trajectory Planning

To determine the time required to complete the move, the velocity curve is integrated over the total move profile:

$$d = \int v dt = \int_{t0}^{t1} at dt + \int_{t1}^{t2} v_s dt + \int_{t2}^{t3} (at_3 - at) dt$$

Solving for t_3:

$$t_3 = \frac{d}{v_s} + \frac{v_s}{a} \tag{35}$$

This time is used to calculate the angle with which to lead the spindle:

$$L = \frac{360}{2\pi} \cdot \omega \cdot t_3 \tag{36}$$

Note that the lead angle and push distance are interdependent, so the solution requires iteration. Convergence is not proven, but absolutely observed in the tooling system.

Self-Modification

At low pushing amplitudes (less than 200μm), a divergence between commanded and actual ring displacements is observed. This effect can be due to several factors:

- Departure of the empirical velocity model from the "ideal" friction model. As true friction is time- or history-dependent and highly nonlinear in the low-amplitude/low-velocity regime, the simplified model presented cannot account for all effects.
- Compliance in the mechanical system, including compliance of the part, spindle, pusher tip, linear slide, and mounting fixtures.
- Servo system compliance due to the inability of the integral gain control to act quickly enough during very short duration motion trajectories
- Noise or improper filtering of the measurement signal.
- Other physical noise inherent from material transfer (*e.g.*, dust, lubricant) into and out of the system.

To compensate for these effects, a simple computational mechanism is employed in the form of an offset P added to the calculated push distance. The offset function is recursive and has two components:

$$\begin{aligned} P_{k+1} &= P_k + d_{remain} + d_{stroke} \\ P_0 &\equiv 0 \\ d_{remain} &\equiv remaining\ \ gap\ to\ be\ closed \\ d_{stroke} &\equiv residual\ \ dist.\ error\ \left(actual - commanded\right) \end{aligned} \tag{37}$$

The remaining gap compensation is calculated when the pusher fails to contact the part (subsequent ring models differ by less than 5% of the last desired push distance). This is the difference between the known probe position at full closure and the instantaneous probe position at the end of the push stroke:

$$d_{remain} = d_{probe,pushtip} - d_{probe,push} \tag{38}$$

The stroke compensation is calculated by the difference between the commanded and actual ring movement distances:

$$d_{stroke} = d_{k-1} - d_{actual} \tag{39}$$

$$d_{actual} = \sqrt{r_1^{\,2} + r_2^{\,2} - 2r_1 r_2 \cos(\theta_2 - \theta_1)}$$

Current Results

The current centering tolerance target of 2.5µm between the center of ring geometry and the center of rotation is consistently being met in less than one minute for rings in the range of 0.75 to 1.5kg. This time includes slide advance and initial modeling cycles.

Results of trials for three different ring types are presented in Figure 13, Figure 14, and Figure 15. In each case, the rotational speed is 20 rpm and the centering tolerance is 2.5µm. For Part 1, the tolerance is achieved in 35 seconds with a single overshoot of 20µm. For Part 2, a larger diameter

and more thin-walled part, the tolerance is achieved in 42 seconds with two overshoots of 12μm. For Part 3, the tolerance is achieved in 35 seconds with a single overshoot of 7μm.

Successful centering has been achieved at speeds of up to 45 rpm, but such results lack consistency due to current control and data loop rates.

In this paper, we have presented a flexible tooling system as a feasible alternative to current hard tooling or manual centering for use in rotationally symmetric part metrology and center-critical processing. Such a system avoids error and inconsistency of the human machine, and changeover time of hard tooling for varying part types.

Conclusions and Future Work

The current flexible tooling system employs only a single fixed pusher tip and single-point measuring device. These characteristics make it flexible in being applied to varied part sizes with negligible setup time. The system is readily adaptable to a range of part sizes, masses and vertical contours with only internal variable changes. The system has been designed for ready integration into existing manufacturing and metrology equipment. We are now considering a number of improvement efforts.

Partial Revolution Modeling

Currently, the ring surface is modeled using a full revolution of sample data. From this model, the best-fit ring eccentricity amplitude and direction are extracted. In the interest of decreasing cycle time, a partial revolution model will be developed which estimate the eccentricity amplitude and direction for coarse pushing attempts with a smaller, partial revolution, data set. This development is in conjunction with hardware upgrades for higher data density.

Improved Friction and Impact Modeling

Currently, the self-modification portion of the algorithm accounts for shortcomings in the empirical velocity equation used to compensate for friction. This provides for instantaneous adjustment of the process, but no accounting of history or prediction of future behavior. To these ends, a more accurate friction and impact model applicable to small amplitude actuation distances will be developed and implemented in the algorithm.

Parametric Variable Identification

Future efforts related to flexibility among ring types and families will be focused on defining and modeling the contribution of part-specific variables such as mass, contact face area and contact surface characterisation. Precise modeling of these variables will reduce the need

for the previously described compensation scheme, and thus the convergence time of the centering process.

Controller Design

Another area of future research will be in advanced controller design. As the system is applied to heavier rings, we expect system compliance to become appreciable and reduce the effectiveness of our linear controller. In this case, we plan to investigate sliding mode control, gain scheduling based on ring characteristics, and nonlinear control schemes better able to react to high force gradients when actuating large parts.

Hardware Improvement

A final area of focus is in control hardware improvement. The system is currently implemented through a compact chassis PXI bus with dedicated motion control. Current control loop rate is near 100 Hz, undesirably slow for this application, but this should be greatly improved in conjunction with controller design upgrades. We plan to implement the system directly on Field Programmable Gate Array (FPGA) hardware, which will allow custom control and I/O design, loop rates in a more desirable range (10-20kHz expected), as well as reduction of overall system cost for integration.

Acknowledgements

We wish to express gratitude to the Timken Company for funding this research and for providing prototype equipment components, and also to National Instruments for funding this research in part and for providing control hardware and software.

References

Alvarez-Ramírez, J.; Garrido, R.; Femat, R. "Control of systems with friction," *Physical Review E (Statistical Physics, Plasmas, Fluids, and Related Interdisciplinary Topics)*, v 51, n 6, pt.B, June 1995, p 6235-8.

Åström, Karl Johan, "Control of Systems with Friction", Fourth International Conference on Motion and Vibration Control, MoViC, pp. 25–32, Zurich, Switzerland, August 1998.

Dupont, P.E. "Avoiding stick-slip in position and force control through feedback ," Proceedings. 1991 IEEE International Conference on Robotics and Automation (Cat. No.91CH2969-4), 1991, p 1470-5.

Dupont, Pierre; Armstrong, Brian; Hayward, Vincent. "Elasto-plastic friction model: contact compliance and stiction ," Proceedings of the American Control Conference, v 2, 2000, p 1072-1077.

Ferrero, J.F.; Barrau, J.J. "Study of dry friction under small displacements and near-zero sliding velocity ," *Wear*, v 209, n 1-2, Aug, 1997, p 322-327.

Hirschorn, R.M.; Miller, G. "Control of nonlinear systems with friction ," *IEEE Transactions on Control Systems Technology*, v 7, n 5, Sep, 1999, p 588-595.

Huang, Wesley H.; Krotkov, Eric P.; Mason, Matthew T. "Impulsive manipulation," Proceedings - IEEE International Conference on Robotics and Automation, v 1, 1995, p 120-125.

Huang, Wesley H.; Mason, Matthew T. "Limiting Cases of Impulsive Manipulation," Robotics Institute, Carnegie Mellon University, Report CMU-RI-TR-96-24, 1996.

Huang, Wesley H.; Mason, Matthew T. "Mechanics, planning, and control for tapping," *International Journal of Robotics Research*, v 19, n 10, Oct, 2000, p 883-894.

Kalman, R.E. "New approach to linear filtering and prediction problems," *American Society of Mechanical Engineers Transactions of Journal of Basic Engineering Series D*, v 82, n 1, Mar, 1960, 59-IRD-11, p 35-45.

Liu, Yung-Tien; Higuchi, Toshiro; Fung, Rong-Fong. "A novel precision positioning table utilizing impact force of spring-mounted piezoelectric actuator - Part I: Experimental design and results ," *Precision Engineering*, v 27, n 1, January, 2003, p 14-21.

Lynch, K.M. "Estimating the friction parameters of pushed objects," IROS '93. Proceedings of the 1993 IEEE/RSJ International Conference on Intelligent Robots and Systems. Intelligent Robots for Flexibility (Cat. No.93CH3213-6), 1993, p 186-193.

Lynch, K.M. "Locally controllable manipulation by stable pushing ," *IEEE Transactions on Robotics and Automation*, v 15, n 2, April 1999, p 318-27.

Lynch, K.M. "The mechanics of fine manipulation by pushing ," Proceedings. IEEE International Conference on Robotics And Automation (Cat. No.92CH3140-1), 1992, p 2269-76.

Lynch, Kevin M.; Mason, Matthew T. "Controllability of pushing ," Proceedings - IEEE International Conference on Robotics and Automation, v 1995, p 112-119.

Lynch, K.M.; Mason, M.T. "Stable pushing: mechanics, controllability, and planning ," *International Journal of Robotics Research*, v 15, n 6, Dec. 1996, p 533-56.

Mirtich, B. and Canny, J., "Impulse-based Simulation of Rigid Bodies," Proceedings of the Symposium on Interactive 3D Graphics, 1995, p 181-188.

Olsson, H.; Åström, K.J. "Friction generated limit cycles," *IEEE Transactions on Control Systems Technology*, v 9, n 4, July 2001, p 629-36.

Peshkin, Michael A.; Sanderson, Arthur C. "The Motion of a Pushed, Sliding Workpiece," *IEEE Journal of Robotics and Automation*, Vol. 4, No. 6, December 1988, p. 569.

Siebenhaar, Christian. "Precise adjustment method using stroke impulse and friction," *Precision Engineering*, v 28, n 2, April, 2004, p 194-203.

Welch, G. and Bishop, G. "An introduction to the Kalman filter". Technical Report TR95-041, Department of Computer Science, University of North Carolina - Chapel Hill, May 2003.

de Wit, C. Canudas; Olsson, H.; Åström, K.J.; Lischinsky, P. "New model for control of systems with friction ," *IEEE Transactions on Automatic Control*, v 40, n 3, Mar, 1995, p 419-425.

Yao, Wenli; Chen, Bin; Liu, Caishan. "Energetic coefficient of restitution for planar impact in multi-rigid-body systems with friction ," *International Journal of Impact Engineering*, v 31, n 3, March, 2005, p 255-265.

Zesch, Wolfgang; Fearing, Ronald S. "Alignment of microparts using force controlled pushing ," Proceedings of SPIE - The International Society for Optical Engineering, v 3519, 1998, p 148-156.

Figures

Figure 1 - Prototype System: Spindle, Linear Slide, Measurement Probe, Pusher Tip

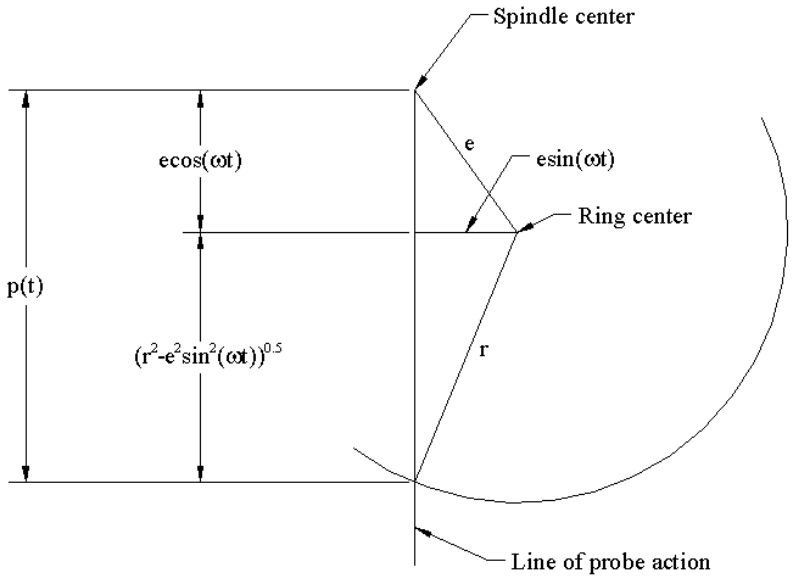

Figure 2 - Parameters for Ring Velocity Derivation

Author

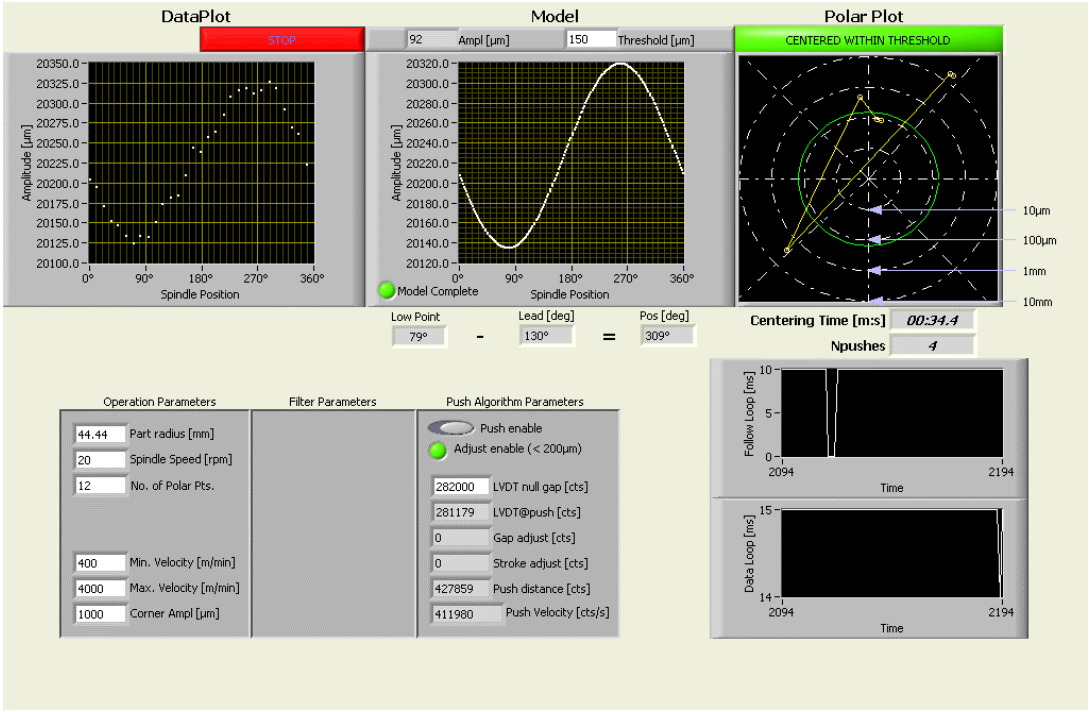

Figure 3 - User Interface of Centering System

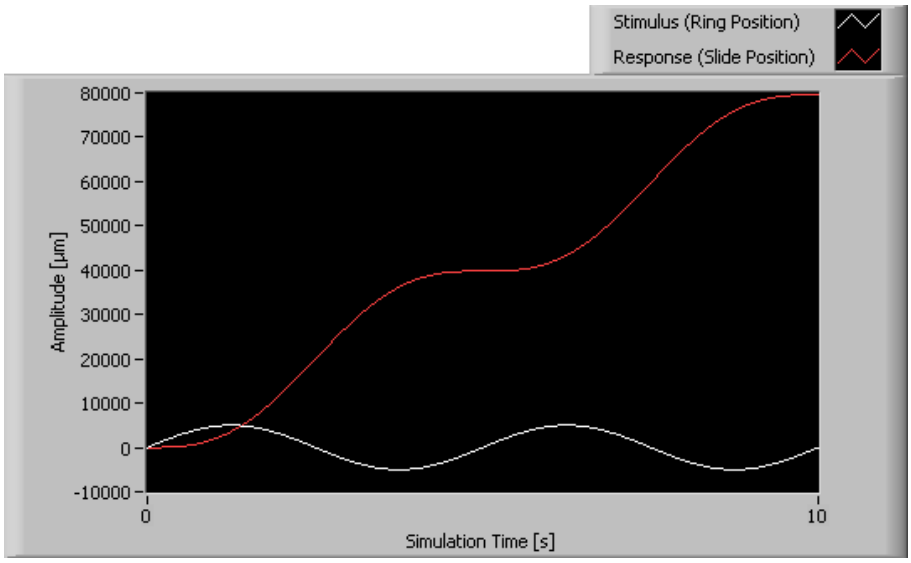

Figure 4 – Time Response of Uncontrolled System (0.2Hz Sine Wave Input)

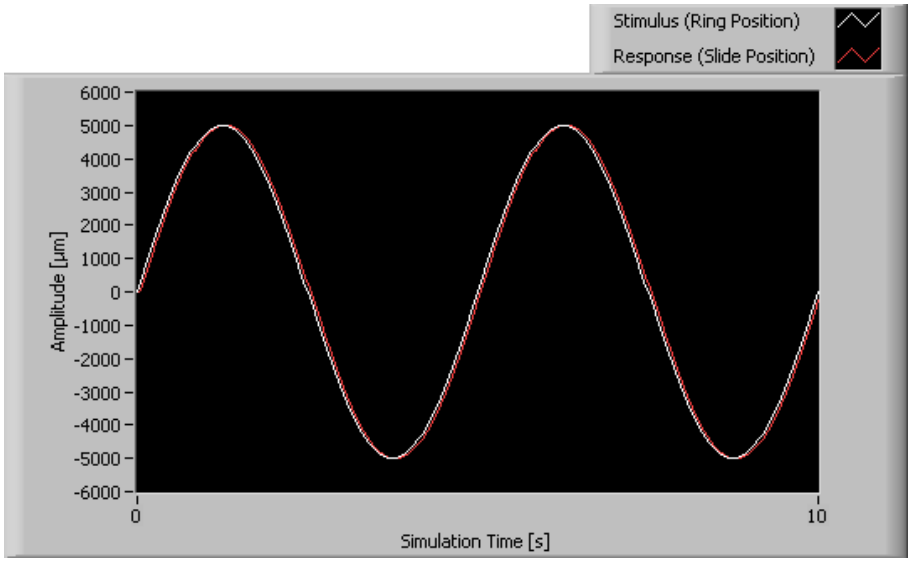

Figure 5 – Time Response Plot of Controlled System (0.2Hz Sine Wave Input)

Author

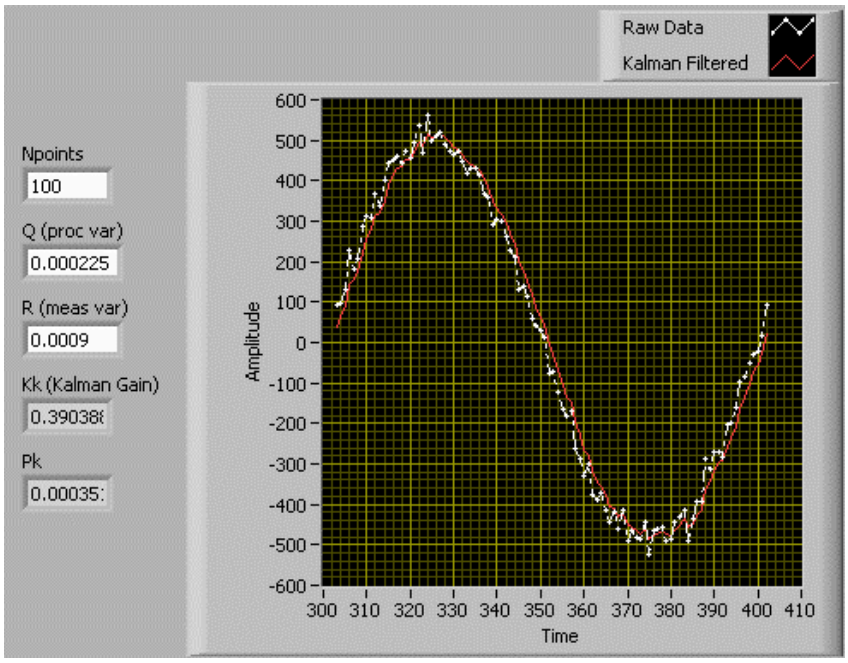

Figure 6 - Kalman Filter Performance on a Noisy Signal

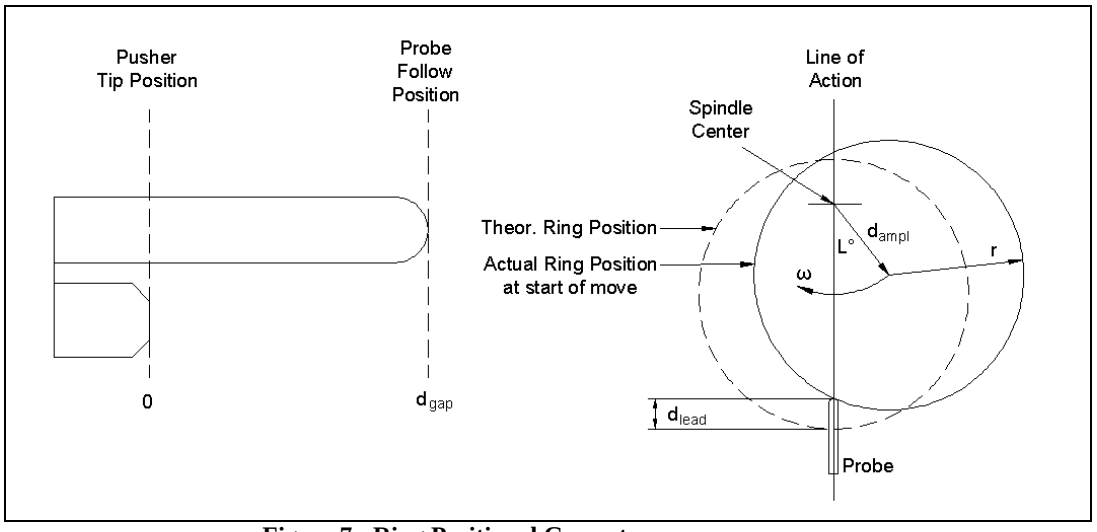

Figure 7 - Ring Positional Geometry

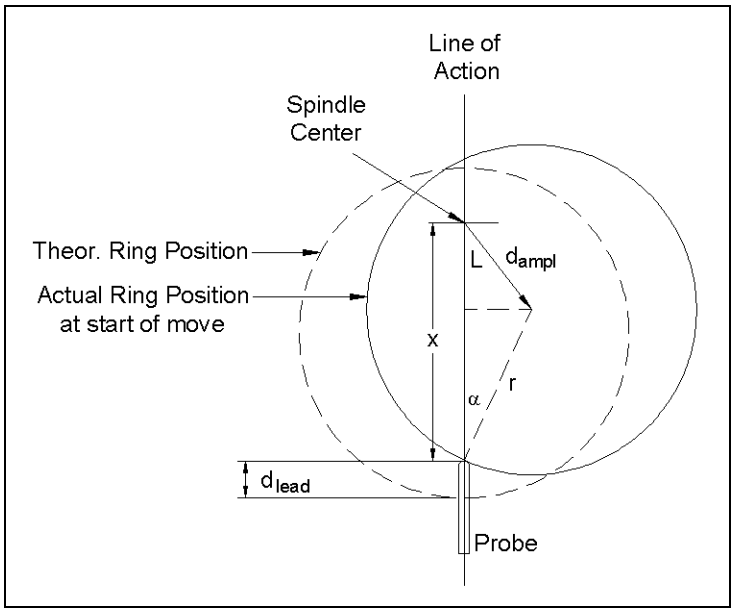

Figure 8 - Ring Lead Geometry

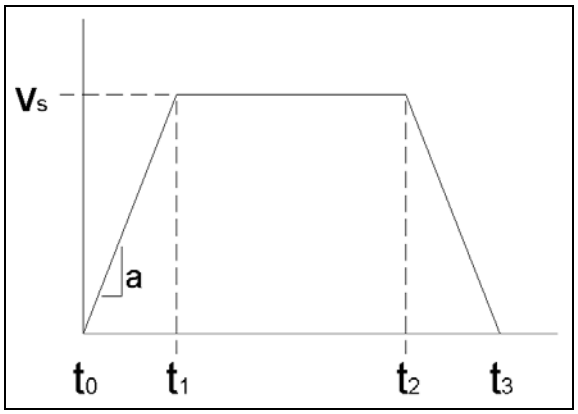

Figure 9 - Velocity Profile of Actuation Move

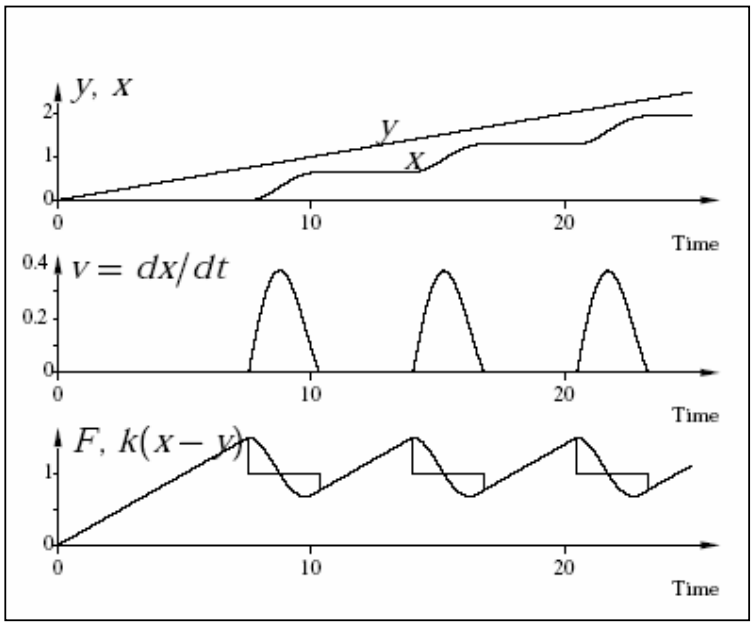

Figure 10 - Simulation of Stick-Slip Motion of Spring y pulling Mass x (Åström 98)

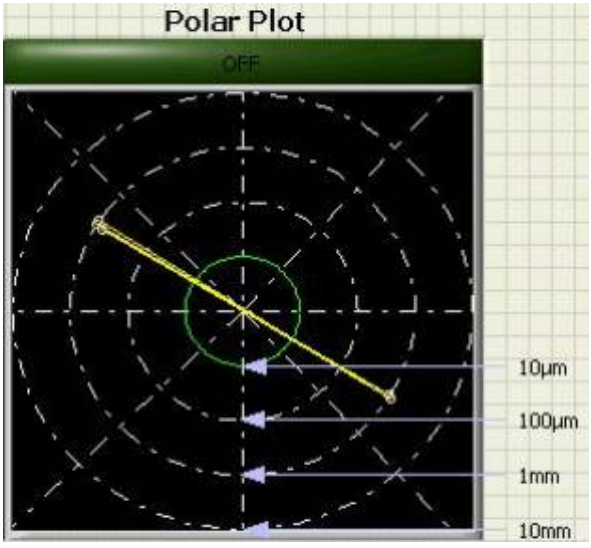

Figure 11 - Limit Cycle of Actuation Across Tolerance Zone

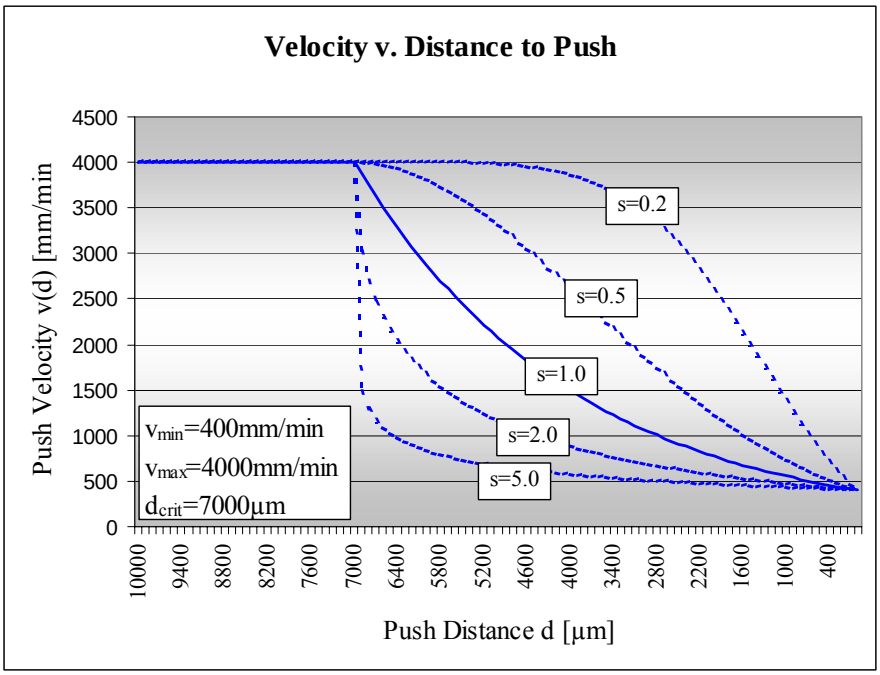

Figure 12 - Pushing Velocity Function (s = steepness)

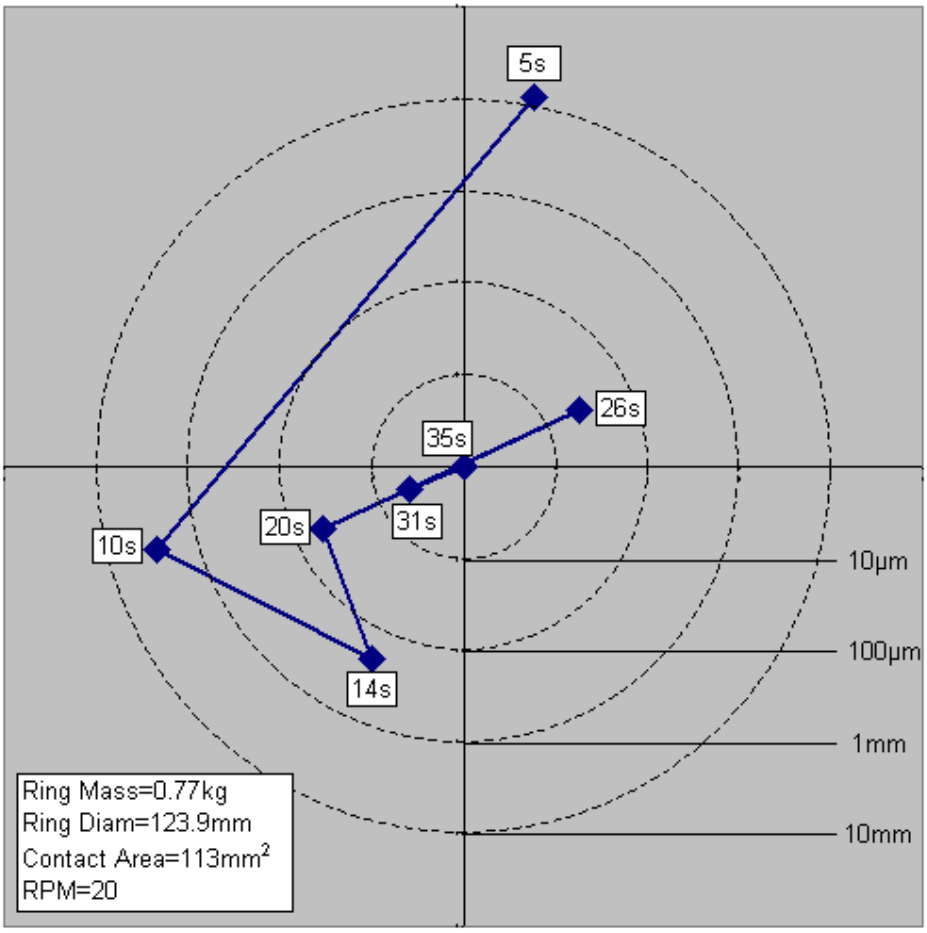

Figure 13 –Centering Cycle for Part 1

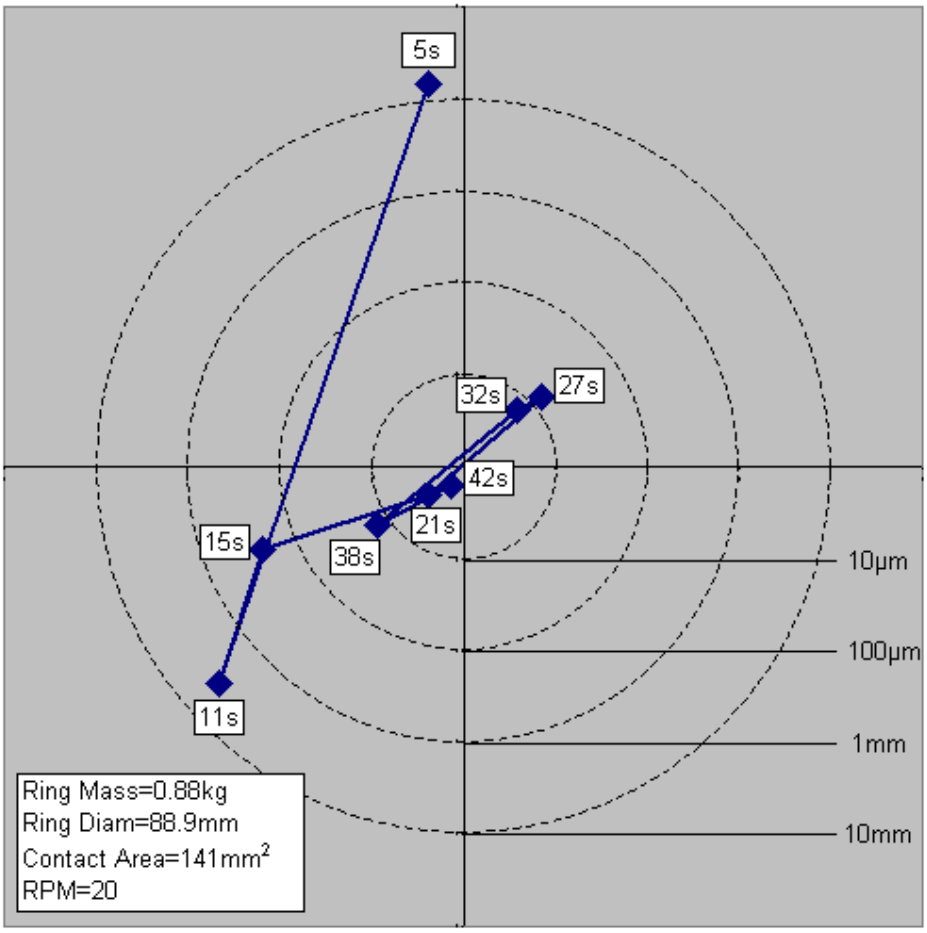

Figure 14 –Centering Cycle for Part 2

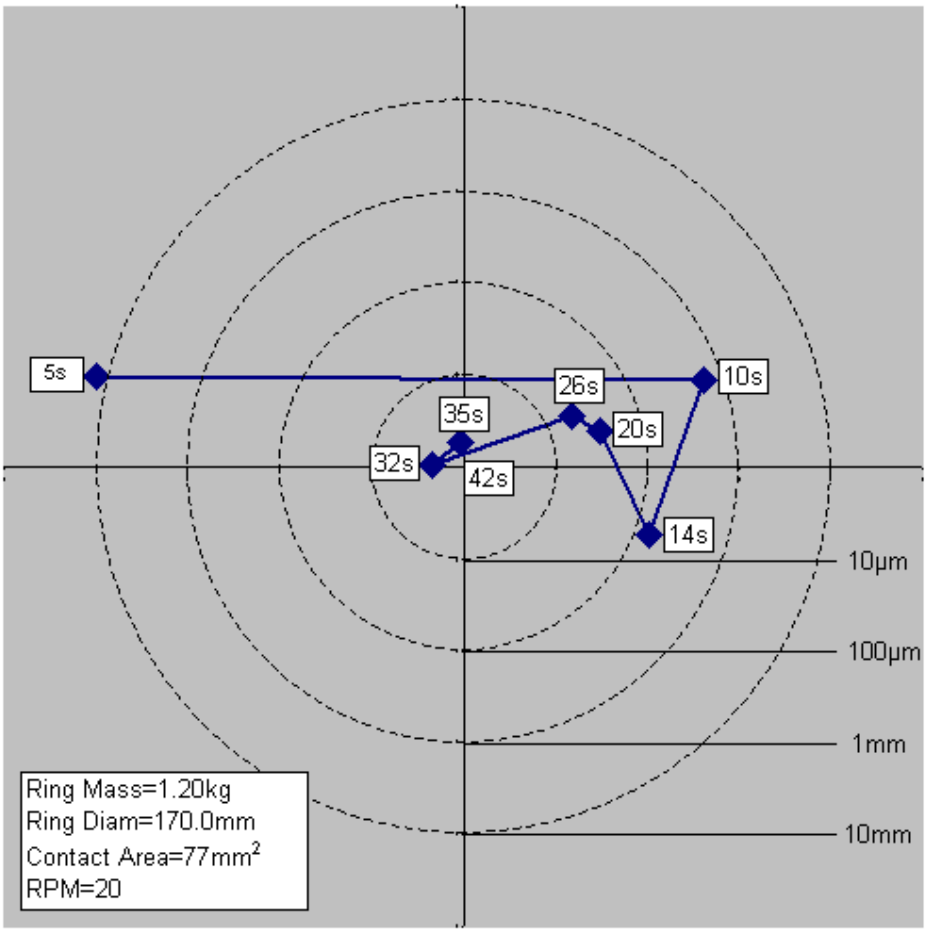

Figure 15 –Centering Cycle for Part 3